PHYSICAL REVIEW A VOLUME 27, NUMBER 3 MARCH 1983

Radiation energetics of a laser-produced plasma

D. Duston, R. W. Clark, J. Davis, and J. P. Apruzese
Plasma Radiation Branch, Plasma Physics Division, Naval Research Laboratory, Washington D.C. 20375

(Received 16 August 1982)

The energy transport in a laser-heated thin foil is investigated with the use of a detailed radiation-hydrodynamic model. The calculation is performed for a long laser pulse (3 nsec full width at half maximum) at relatively low irradiance (10^{13} W/cm^2), incident on an 8-μm-thick aluminum foil, and results confirm earlier experimental hypotheses that the dense plasma at the rear side of the foil is heated predominantly by radiation. The model couples a one-dimensional, planar hydrodynamic calculation with a detailed description of the radiation-ionization dynamics in a totally self-consistent manner, thereby assuring that the dominant physical processes determining the energy transport are characterized accurately. The specific radiative mechanisms responsible for energy transfer from the front to the back surface of the foil are found to be quite complex and are described in detail. The front and rear spectral emission are presented and discussed from the point of view of both energetic and diagnostic considerations. Shifting absorption edges due to ionizing plasma are shown to be responsible for many interesting phenomena affecting the energy transport. Time integration of the K-shell spectral features is also studied and its effects on the temperature and density diagnostics are analyzed. Finally $K\alpha$ emission lines are shown to be a promising new diagnostic in determining the time development of the temperature near the foil ablation surface.

I. INTRODUCTION

Recent experiments[1-7] involving the laser heating and subsequent ablative acceleration of thin foil targets have been performed to demonstrate that velocities necessary for sufficient compression of laser-fusion fuel can be attained with present technology. Also of great interest is the degree of preheat of the fuel[8] preceding the main compression phase in inertial confinement fusion experiments. This preheat is due to a number of effects, viz., suprathermal electrons, strong shocks, thermal conduction, and radiation. It has been suggested[2] that the degree of preheat can be assessed from the foil rearside temperature in laser-foil experiments. In addition, measurement of the rearside temperature provides information useful in determining the dominant heating process.

In an effort to explain the details of the relevant physics involved in laser heating of thin foils, we have investigated this phenomenon with a hydrodynamic model designed to reliably calculate the radiation physics in more detail than has been hitherto attempted. The competing processes of energy transfer are studied for a low-irradiance, long-pulse laser beam in order to quantitatively verify, as experimental evidence indicates, that radiative heating is the dominant transport mechanism to the foil backside under these conditions. It is neither our intent nor purpose to corroborate or criticize conclusions drawn from previous measurements. However, comparisons will be made with experimental results whenever possible to provide insight into the role played by radiation in laser-foil heating.

In studying the laser heating of a thin foil, we discuss several interesting phenomena affecting energy transport. Although an abundant amount of radiation is emitted via K-shell lines in the plasma blowoff region of the ablating foil, the mechanism of down-conversion in photon frequency as photons are absorbed and reemitted deeper into the plasma was found to play a major role in the backside heating. The relative timings of laser pulse, backside emission, and backside temperature behavior show interesting but puzzling relationships in the experimental results, and this theoretical study offers explanation for all of these observations. Our investigation of so-called "foil burn-through" shows that an ionization wave can propagate through the plasma (much like a combustion wave), causing shifts in inner-shell photon absorption edges and strongly time-dependent energy transport in the dense plasma regions. We attempt to explain the details of these radiative mechanisms and the way in which they affect the energy transport in the target and escaping photon emission. Since the results of a calculation of this type depend critically on the theoretical model employed, the details of this model are discussed in depth in the section that follows.

II. THEORETICAL MODEL

For discussion purposes, the model can be conveniently partitioned into three aspects: (i) hydrodynamics and laser absorption, (ii) ionization and atomic physics, and (iii) radiation emission and transport. Many of the finer details of the method of solution of the relevant equations have been discussed at length in previous work. These studies are referenced where applicable, but the model is described accurately below in order to present a complete picture of the investigation reported on here.

A. Hydrodynamics and laser absorption

The basic hydrodynamic variables of mass, momentum, and total energy are transported in one dimension using a numerical scheme with a sliding-zone version of flux-corrected transport.[9] A special gridding algorithm is used which moves zones in a Lagrangian fashion and adjusts the mesh in order to resolve steep gradients in the flow. The hydrodynamic equations solved are

$$\frac{D\rho}{Dt}=\frac{\partial\rho}{\partial t}+\frac{\partial}{\partial x}(u\rho)=0\ , \tag{1}$$

$$\frac{D(\rho u)}{Dt}=-\frac{d\bar{p}}{dx}\ , \tag{2}$$

$$\frac{D\epsilon_T}{Dt}=-\frac{\partial}{\partial x}(u\bar{p})+\dot{\epsilon}_{\text{rad}}+\dot{\epsilon}_{\text{dep}}+\frac{\partial}{\partial x}\left[\eta N\frac{\partial}{\partial x}T\right]\ , \tag{3}$$

where ρ is mass density, u is velocity, $\bar{p}$ is pressure, ϵ_T is total energy, $\dot{\epsilon}_{\text{rad}}$ is the rate of energy loss or gain due to radiation, $\dot{\epsilon}_{\text{dep}}$ is the rate of energy gain due to the laser deposition process, η is the thermal conductivity, and N is the ion density. The thermal conductivity is calculated implicitly, using an iterative Crank-Nicholson scheme. For each finite difference time-step, the temperature and temperature-dependent conductivities are iterated on until the maximum local relative error is less than one percent.

Since densities did not much exceed solid density in this study, a simple equation of state was assumed with

$$\bar{p}=\tfrac{2}{3}(\epsilon_T-\tfrac{1}{2}\rho u^2-\epsilon_I)\ , \tag{4}$$

where ϵ_I is the ion potential energy due to ionization and excitation. A single temperature model was employed where

$$kT=\frac{\bar{p}}{(\rho/m_I)(1+\bar{z})}\ , \tag{5}$$

where m_I is ion mass, T is temperature, and $\bar{z}$ is the effective ion charge. The ionization energy, ϵ_I, radiation energy, ϵ_{rad}, and effective charge, $\bar{z}$, are calculated from the ionization-radiation equations and are explained below. A single temperature assumption is valid in the cold dense target as well as in the laser deposition region, since thermal equilibration times are short compared with the time scales of the energy input and changes in the hydrodynamic variables. It is not a very good approximation in the hot, tenuous blowoff region of the frontside, but since the density of this region is relatively low, it is expected to have a negligible effect on the energy transport to the rear of the foil.

Since the main motivation for this study was to investigate the role of radiation in the energy transport and not to study the laser absorption mechanism in detail, the laser energy deposition was modeled via classical inverse bremsstrahlung. The absorption coefficient used in the calculation is defined in the usual way,

$$\kappa_{\text{IB}}=\frac{\omega_{pe}^2}{\omega^2 ct_{ei}(1-\omega_{pe}^2/\omega^2)^{1/2}}\ , \tag{6}$$

where ω_{pe} is the electron plasma frequency, t_{ei} is the electron-ion collision time, and ω is the laser frequency. For simplicity, the asumption was also made that any incident radiation not absorbed before reaching the cell containing the critical surface was dumped in that cell; hence, no reflection of the laser radiation was allowed. This means that these results would be more appropriately compared to experiments with laser irradiances slightly higher than the theoretical value used here, since we, in effect, assume 100% absorption of the incident energy.

The laser pulse was assumed to have a time dependence approximating a Gaussian shape with a full width at half maximum of about 3.0 nsec and reaching a peak intensity of 10^{13} W/cm^2 at a time of 4.0 nsec after initiation of the simulation. The laser wavelength was 1.06 μm, modeling the input from a Nd:glass laser driver. The time history of the laser power is shown in Fig. 4.

B. Ionization model

The atomic model used in determining the plasma ionization and excitation state has been presented elsewhere,[10] and a more complete description can be found in that work. A set of atomic rate equations of the form

$$\frac{df_i}{dt}=\sum_j W_{ji}f_j-\sum_j W_{ij}f_i \tag{7}$$

is used to characterize the ionic populations in the plasma. Here, f is the fractional population of level i, and W_{ji} is the reaction rate describing the collisional processes from initial state j to final state i. An equation of this type is constructed for each of the atomic levels included in the model. In this calculation we considered the plasma to be in collisional-radiative equilibrium (CRE),[11] making the assumption that the plasma ionization state is immediately responsive to changes in hydrodynamic quantities [the explicit time dependence is omitted in Eq. (7)]. This assumption is an excellent one in the high-density regions of the plasma (behind the laser critical surface), where particle-particle collision times are extremely short, but it is a marginal assumption in the hot, rarefied blowoff region. Since the temperature of the blowoff rises quickly to almost 1 keV and is maintained at this value (where K-shell ions are the dominant species) for several nanoseconds, little ionization or recombination takes place on even a 10-nsec time scale after the peak in the laser pulse. Hence, we have chosen to apply the equilibrium condition everywhere in this study. Preliminary results from a study of time-dependent effects on the ionization state in laser plasmas indicate slight effects on the frontside emission, but we leave the details of that investigation for future work.

The atomic level structure employed in this model includes all 14 ground states of aluminum plus 84 selected excited states, somewhat evenly distributed from Al III to Al XIII (the details of the level structure and energy level values are found in Ref. 10). With such an extensive atomic structure, the level distribution of the plasma can be accurately described from temperatures of a few eV to several keV. The excited-state structure included in this study was selected to best represent the radiation energetics for the plasma conditions under investigation, and we believe that this model takes into account almost all of the energetic transitions required to accurately describe the emission resulting from laser-foil interaction phenomena.

The rate coefficients that are used to calculate the populating and depopulating rates, W_{ji}, are calculated using various scattering techniques. The processes included in this calculation and the methods used in calculating the corresponding rate coefficients are summarized below.

(1) *Collisional ionization*—exchange classical impact-parameter (ECIP) method[12] (the effect of autoionizing resonances on the cross sections has been ignored).

(2) *Photoionization*—hydrogenic approximation with Karzas-Latter Gaunt factors.[13,14]

(3) *Dielectronic recombination*—the detailed calculations of Jacobs *et al.*[15] are used.

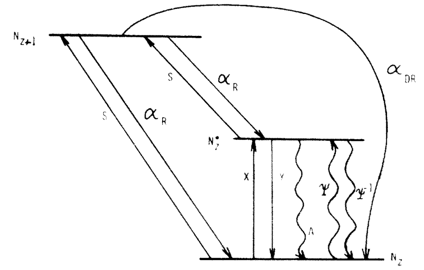

FIG. 1. Simple three-level diagram used to depict the atomic processes included in this ionization model. S is collisional and photoionization, α_R is radiative recombination and three-body recombination, α_{DR} is dielectronic recombination, X is electron collisional excitation, Y is collisional deexcitation, A is spontaneous decay, and ψ and ψ^{-1} are stimulated absorption and emission.

(4) *Collisional excitation*—Coulomb-Born distorted-wave approximation including exchange effects,[16] or the semiclassical impact-parameter (SCI) technique.[17]

(5) *Spontaneous radiative decay*—oscillator strengths are taken from several calculations and measurements.[10]

(6) *Photoexcitation*—oscillator strengths used are those quoted above to determine optical depths (see the next section on radiation transport).

Finally, collisional and radiative recombination, collisional deexcitation, and stimulated emission are all calculated as the detailed balance of the corresponding opposite rate listed above. A simplified level diagram using two ground states and a single excited state is shown in Fig. 1 to show schematically the collisional processes included in the model.

An important question to be addressed regarding the rate coefficients is how well the cross sections are known, since the radiative emission is strongly influenced by this accuracy. An extreme upper limit of a factor of 2 can be globally placed on the rates. However, most of them are correct to much better accuracy, particularly electron-impact ionization, collisional excitation, and the oscillator strengths. A complete referencing of these coefficients can be found in other papers.[18,19]

Once the set of rate equations (including the radiation transport) has been solved for the level populations, f_i, the electron density can be calculated,

$$N_e = \sum_i z_i f_i N_I \ , \tag{8}$$

where z_i is the ionic charge of level i and N_I is the total ion density.

The ionization and excitation energy can also be calculated by

$$\epsilon_I = \sum_i \chi_i f_i N_I \;, \tag{9}$$

where χ_i is the energy of level i, measured from the ground state of the neutral atom.

C. Radiation emission and transport

The radiation emission from plasmas is strictly dependent on the atomic level population densities. Once these state densities are accurately known, the radiative source functions can be calculated directly. Except for optically thin plasmas, however, the level populations also depend on the radiation field since optical pumping of states by photon reabsorption can cause significant redistribution of the populations, not only from ground to excited states but between ionization stages via both photoionization and electron-impact ionization of excited states whose populations have been enhanced by photoexcitation. Thus, the ionization and radiation equations are strongly coupled and must be solved self-consistently. In this model, this is done iteratively by first calculating the level populations at a time step using the radiation field from the previous time step, then using these populations to calculate a new radiation field and recalculating populations until convergence is reached. Any technique which does not allow for this important optical pumping of the levels is unsatisfactory, since this feedback mechanism can be critically important for both energetic and diagnostic accuracy.

The transport scheme used in this study is based on a probability-of-escape for the photons.[20] The transport method for photon absorption by valence electrons is described first. For line photons, the probability is determined by the line shape; for a Doppler profile at large optical depth,

$$P_e \simeq [\tau_0(\pi \ln \tau_0)^{1/2}]^{-1} \;, \tag{10}$$

while for a Voigt profile,

$$P_e \simeq \tfrac{2}{3}(a_{ij}/\tau_0)^{1/2} \;, \tag{11}$$

where τ_0 is the line center optical depth and a_{ij} is the Voigt damping parameter

$$a_{ij} = \frac{\sum_k A_{ik} + \sum_k C_{ik} + \sum_k A_{jk} + \sum_k C_{jk}}{4\pi\Delta\nu_D} \;. \tag{12}$$

Here, A and C are radiative and collisional depopulation rates of the lower and upper levels, i and j, of the radiative transition. Since the Voigt profile reduces to a Doppler core at low densities, the model calculates both probabilities and uses the largest value (see Ref. 20 for a fuller discussion). An expression has recently been developed for Stark profiles within the probability-of-escape formalism but it has not yet been implemented in our model.

Continuum photons due to radiative recombination processes are also transported by probability-of-escape techniques. An emission profile of the form

$$\phi_e \sim \exp[-h(\nu-\nu_0)/kT] \tag{13}$$

is assumed with an absorption profile of the form

$$\phi_a \sim (\nu_0/\nu)^3 \;, \tag{14}$$

where ν_0 is the frequency of the continuum edge. The exact probability integral

$$P_e = \frac{\int \phi_e e^{-\tau_0\phi_a} d\nu/\nu}{\int \phi_e d\nu/\nu} \tag{15}$$

has been solved for a wide range of values for τ_0 (the optical depth at the edge) and $h(\nu-\nu_0)/kT$; the results have been fit to Chebychev polynomials and are then reconstructed on-line in the model. The free-free emission is transported by solving the equation of transfer explicitly over a grid of photon frequencies; this can be done efficiently because of the smooth nature of the emission function. To calculate the absorption coefficient, the following expression is used[21]:

$$\kappa_{ff}(\nu) = (\text{const}) N_e N_I T^{-1/2} \times \sum_i z_i^2 f_i \left[\frac{1-\exp(-h\nu/kT)}{\nu^3} \right] . \tag{16}$$

Then, by integrating over frequency, probabilities of escape from zone to zone can be calculated in a straightforward fashion.

The methods described above deal with photon absorption by valence electrons through photoexcitation or photoionization. However, effects due to inner-shell photon absorption must also be taken into account. This is particularly important for laser-foil interaction models, since the neglect of these processes leads to a gross underestimate of the x-ray deposition in the cold, dense plasma regions, as would be seen by the presence of intense, unattenuated lines and continua in the calculated backside spectrum. Thus, what is potentially the major energy transport mechanism to the backside would be omitted.

In this model, each emission line or continuum edge characterized by the ionization model is attenuated by an inner-shell opacity as well as the valence electron line and continuum opacity described above. The inner-shell photoionization cross section for neutral aluminum is taken from the fits by Biggs and Lighthill,[22] and the inner-shell optical depth can be calculated in a straightforward manner from

$$\tau_{\mathrm{IS}}=\sum_{n}\sigma_{\mathrm{PI}}d_nN_n \ , \tag{17}$$

where σ_{PI} is the photoionization cross section for inner-shell processes, d_n is the zonal path length, and N_n is the zonal ion density.

In general, the dense plasma which strongly attenuates photons via collisions with inner-shell electrons is *not* neutral, and to accurately account for x-ray deposition in the rearside of the foil, the cross section must be adjusted as a function of ionization state as well as photon energy. We have chosen to use the numerical values of the neutral aluminum cross sections and simply shift the M, L, and K absorption edges with ionization state. This is a good approximation for electrons occupying the 1s, 2s, and 2p inner shells for medium- and high-Z materials.[23] A plot of the photoionization cross sections versus photon energy for the different ionization stages of aluminum is shown in Fig. 2. The position of the various absorption edges was taken from the Hartree-Fock calculations of Clementi and Roetti.[24] Note the importance of the edge shift with ionization state; the K edge lies below the Al XII resonance line energy of 1.598 keV (one of the strongest emission lines) for Al I-Al III, and above it for higher ionization stages. Thus, as the backside heats up, the inner-shell optical depth of this line can drop by an order of magnitude and significantly decrease the x-ray heating rate.

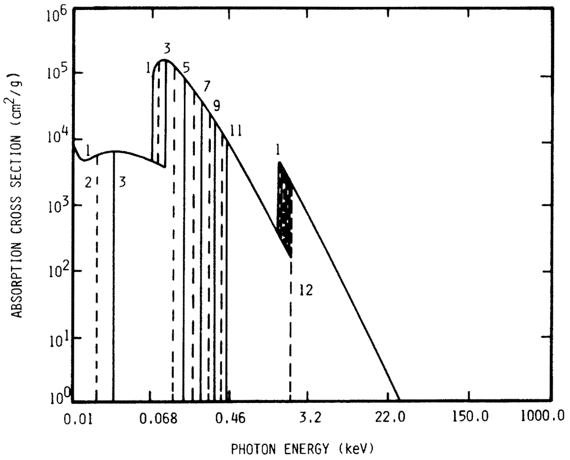

FIG. 2. Inner-shell photoionization cross section versus photon energy for aluminum. Numbers refer to the absorbing atom or ion ($5\equiv$Al V or Al^{4+}).

One advantage of using an ionization model which explicitly calculates the level populations is that the inner-shell attenuation of photons can be calculated state by state rather than using a zonal effective charge to determine the cross section. As a simple illustration, consider Al XII resonance line photons (1.598 keV) incident on a dense zone in the foil backside in which the ions consist of $\frac{1}{3}$ Al III, $\frac{1}{3}$ Al IV, and $\frac{1}{3}$ Al V. The effective ionization is $Z_{\mathrm{eff}}=3$; hence if one were to use a more simplistic calculation of Z_{eff}, the K edge would seem to be shifted to the position corresponding to Al IV at 1.626 keV, above the resonance line photon energy, and the opacity would be reduced markedly. Thus, the K-line attenuation which actually occurs in that zone by the 33% Al III concentration would not be taken into account, and the heating rate would be underestimated severalfold if only an average zonal charge were used. Knowledge of the state distributions in the dense plasma regions is therefore often necessary for accurate energy transport. The technique by which inner-shell and valence electron opacities are combined to determine a total probability-of-escape is too detailed to present here and can be found in a separate work.[25]

Using the above expressions, coupling constants linking each numerical zone to every other zone are calculated for each line or recombination edge, and the photon transport from zone to zone and also escaping the plasma is determined. Thus, the bound-bound emission power is calculated by

$$P_{\mathrm{bb}}=\sum_{m}\sum_{n}N_{mn}A_mF_{mn}\Delta E_m \ , \tag{18}$$

where A_m is the radiative decay rate for line m, N_{mn} is the upper-state population for line m in zone n, ΔE_m is the transition energy, and F_{mn} is the probability factor that a photon from line m, emitted in zone n, escapes to the outer boundary of the plasma. A similar expression can be written for the bound-free emission

$$P_{\mathrm{bf}}=\sum_{m}\sum_{n}N_{mn}\alpha_{mn}N_{en}F_{mn}\chi_m \ , \tag{19}$$

where α_{mn} is the radiative recombination rate coefficient for recombination edge m, N_{en} is the electron density in zone n, χ_m is the ionization energy of edge m, and F_{mn} is the zonal escape probability factor for edge m, similar to that for the lines in Eq. (18).

The free-free radiation is calculated using

$$P_{\mathrm{ff}}=(\mathrm{const})\sum_{n}N_{en}N_{In}T_n^{-1/2}\sum_{i}z_i^{\,2}f_{in}\int\exp(-h\nu/kT_n)F_n(\nu)d\nu \ , \tag{20}$$

where $F_n(\nu)$ is the probability that a photon of frequency ν escapes the plasma from zone n. Hence, the total radiation power emitted from the plasma is

$$P_{\text{rad}} = P_{\text{bb}} + P_{\text{bf}} + P_{\text{ff}} \ . \tag{21}$$

If Eqs. (18), (19), and (20) are rewritten to give the net photon transport from zone n to zone n', instead of that which escapes to the plasma outer boundary, the various radiative loss or gain rates $\dot{\epsilon}_{\text{bb}}$, $\dot{\epsilon}_{\text{bf}}$, and $\dot{\epsilon}_{\text{ff}}$, can be calculated along with the total, $\dot{\epsilon}_{\text{rad}}$, which occurs in the expression for the total energy, Eq. (3). In this way, the net cooling and heating by radiation emission and absorption among the various zones of the plasma is accurately accounted for, and a totally self-consistent radiation-ionization-hydrodynamic calculation can be performed.

D. $K\alpha$ emission

It was shown in the last section that line and continuum spectral features are calculated in this model by explicitly treating the bound-bound and bound-free collisional processes. In this section, a method of calculating $K\alpha$ emission is described which differs slightly from the methods used on other spectral features. Spectral lines identified as $K\alpha$ emission are often seen in experimental spectra when high-energy photons or particles are incident on cold target material.[5,26–33,35] For shorter wavelength lasers, hot-electron generation is suppressed, hence, $K\alpha$ emission may be due predominantly to X-ray reabsorption (see Mizui *et al.*[34] and Nishimura *et al.*,[6] and Yaakobi *et al.*[35]). This is the case considered here; the laser-heated front surface emits energetic x-rays back into the cold foil on the other side of the ablation surface. These photons penetrate the electron shells of low charge state ions and can strip off an inner-shell electron. If the photon energy is sufficiently large, a K-shell vacancy is created, which can be filled by either an Auger (radiationless) transition or by resonance fluorescence. For a K-shell Auger transition, an L-shell electron can decay to fill the K-shell vacancy, with the excess energy going to ionize an outer electron. Fluorescence, on the other hand, occurs when an outer (L- or M-shell, in aluminum), electron decays to fill the K-shell vacancy with the excess energy carried off by a $K\alpha$ photon.[36] A technique to accurately account for these processes in an equilibrium plasma has been described recently by Jacobs *et al.*[37] In our work, however, several simplifying assumptions have been made in modeling the $K\alpha$ emission from laser-foil interactions.

Using the expressions from Sec. II C above describing the inner-shell opacity calculation along with the photon field from the frontside of the foil, we calculate a K-shell vacancy creation rate, V_K, for each plasma zone. Since the photoionization cross section is known as a function of ionization stage as well as photon energy, and the ionic population densities are calculated explicitly by our ionization model, this K-shell vacancy creation rate is determined also as a function of ionization state. The K-shell fluorescence yield, ω_K, the proportion of K-shell vacancies which are filled by fluorescence ($K\alpha$ emission), has been calculated by McGuire.[38] Hence, the intensity of $K\alpha$ photons emitted from zone n and ionization stage z can be calculated simply from the following expression:

$$P_K(n,z) = V_K(n,z)\omega_K(z)\Delta E_K(z) \ , \tag{22}$$

where $\Delta E_K(z)$ is the $K\alpha$ transition energy for ion z. Shown in Table I are the K fluorescence yields and the transition energies for the lowest nine charge states of aluminum.

TABLE I. Transition energies and fluorescence yields for the ionization stages of aluminum included in the $K\alpha$ emission model, taken from McGuire's calculations.

Ionization stage	Transition energies (keV)	Fluorescence yields
Al^{0+}	1.486 99	0.033 3
Al^{1+}	1.487 52	0.046
Al^{2+}	1.488 24	0.045
Al^{3+}	1.488 95	0.043 4
Al^{4+}	1.499 58	0.047 9
Al^{5+}	1.511 64	0.052 2
Al^{6+}	1.525 40	0.061 9
Al^{7+}	1.540 37	0.070 0
Al^{8+}	1.557 01	0.062 3

It has been shown[32] experimentally for aluminum that the $K\alpha$ emission from Al^{0+}-Al^{3+} is usually seen as a single unresolved feature in the spectrum due to the small energy difference (~2 eV) separating the four lines. After the first L-shell electron has been removed, however, the lines from the next ions shift measurably to higher energies due to the significantly reduced screening from the missing L electron. Thus, the remaining lines will be seen in the spectrum at higher energy, well resolved from the main $K\alpha$ peak but still below the Al XII resonance and intercombination lines at about 1.59 keV. It is apparent that these lines are clear indicators of the ionic distribution in the cold backside of the foil; a discussion of this diagnostic in the context of the results of this study is found in the next section.

Although opacity effects may alter the $K\alpha$ emission from the backside plasma, the analysis in the following section assumes that all the $K\alpha$ emission escapes the plasma unattenuated. Using solid densities for aluminum, the photon cross section at 1.5 keV from Fig. 2, and a path length of 8 μm, one calculates the optical depth of the $K\alpha$ lines due to photoionization alone to be of order unity, neglecting the resonant effects present in a warm, ionized plasma. However, we leave the problem of $K\alpha$ photon transport through laser-heated foils for future investigations.

III. RESULTS

In this section, the results of a specific laser-foil interaction experiment are discussed. Since the focus of our interest is in the radiation physics, emphasis is placed on that analysis as opposed to a detailed study of laser deposition, suprathermal electron generation and transport, flux-inhibited transport, etc. Previous studies have shown that the onset of suprathermal electrons and flux-inhibited transport occurs at high laser irradiances.[5] To minimize the effects of these phenomena in this study, a relatively low-irradiance laser pulse, 10^{13} W/cm^2 at 1.06 μm wavelength, was assumed to be incident on a thin (8.0 μm) aluminum foil.

The results of this calculation are presented in four sections. First, a qualitative picture of the fundamental physical processes occurring in this calculation are presented. Second, a more detailed analysis of the energy transfer from laser to thermal energy in the foil is given. Third, the calculated frontside and backside spectra are presented to illustrate the qualitative and quantitative nature of the radiation, considering not only what escapes, but what is trapped internally also. Finally, the $K\alpha$ emission is studied and its role as an indicator of the dense rearside plasma conditions is analyzed.

A. The nature of laser-heated foils

When intense laser radiation strikes a thin medium-z foil, the physical mechanisms which play a role in the transport of that energy are extremely complex. The radiation is absorbed in a relatively thin surface layer, determined by the laser wavelength. The plasma is strongly heated locally by this energy deposition and ablates away from the foil surface creating a large density gradient. Simultaneously with material ablation, energy is transported into the foil by shock heating, thermal conduction, suprathermal electrons, and secondary radiation emission. In order to more clearly explain the results of this calculation, the foil plasma is considered to be comprised of three regions, as shown in Fig. 3. (1) A high-temperature, low-density "blowoff" plasma formed as heated material ablates from the frontside of the foil, (2) a central "transition" zone in which the laser energy is absorbed, characterized by large temperature and density gradients resulting from the local deposition and transport of energy, and (3) a cold, dense "backside" region into which energy is transported from the blowoff and transition zones by one or more of the processes mentioned above.

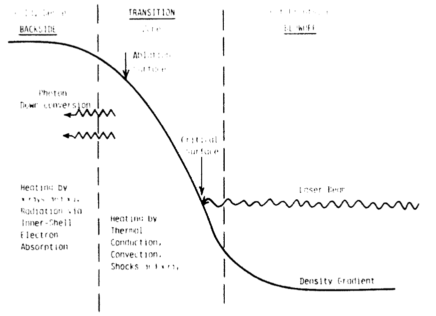

FIG. 3. Simple schematic of the major physical processes taking place in laser-foil interaction at low irradiance, showing the three regions referred to in the text.

Much work has been done in an effort to model plasma heating by thermal conduction, shock and compression waves, and suprathermal electrons, and the physical mechanism of each of these processes is at least qualitatively understood if not, as yet, quantified exactly. Although several workers have studied laser plasmas using hydrodynamic codes coupled with radiation models,[39–43] no detailed study of the role of secondary radiational heating has been reported on in laser-heated foils; hence, we concentrate our investigation on this aspect of the problem.

Laser heating of the plasma in the vicinity of the critical surface ($N \approx 10^{20}$ ions/cm^3 for 1.06 μm laser light in aluminum) results in radiation emission by this heated plasma in both the forward and rear directions. In aluminum, this radiation will consist mainly of soft x-ray and xuv photons. The soft x rays, with energies above 1.5 keV, are emitted from the plasma heated to electron temperatures above at least 250 eV, and result mainly from bound-bound transitions due to excitation of K-shell electrons. The xuv photons, with energies below about 1.0 keV, are emitted from plasma between about 10 and 150 eV and result mainly from bound-free transitions and, to a slightly lesser degree, bound-bound transitions of L-shell electrons, depending on the plasma density. Between photon energies of about 0.5 and 1.5 keV, continuum emission dominates the spectrum; no strong lines are found in this region due to the large difference in excitation energies of L- and K-shell electrons.

The radiation emitted in the forward direction suffers some attenuation due to resonant photoexcitation processes, but most escapes through the low-density blowoff region. That which is emitted back into the foil, however, is strongly attenuated by both valence electron photoexcitation and inner-shell electron photoionization, due to the large optical depths in this dense region. Since the backside plasma is of much higher density and highly collisional, much of this absorbed radiation is collisionally quenched, resulting in increased temperature and ionization of the cold matter. This matter will, of course, reradiate much of its energy, but at lower photon energies corresponding to the dominant ionization stages of the colder material. This process continues throughout the transition and backside regions, with photons being absorbed and reemitted at lower frequencies. Hence, the radiation reaching the rear surface of the plasma is comprised of a wide spectrum of photons, from frontside soft x rays, which manage to penetrate the total extent of the foil, to transition and backside photons which have been born in the xuv range via progressive *down-conversion* in frequency of the incident soft x rays. It is this progressive down-conversion process which makes the radiational heating of the dense backside plasma such a complex process, and renders the simple technique of turning the measured forward spectrum back onto the cold, dense plasma to obtain estimates of the radiational heating, somewhat inaccurate.

The photons born in the transition and blowoff regions and emitted to the rear tend to be absorbed in the dense backside primarily by inner-shell processes. This creates *K*- and *L*-shell vacancies which have to be filled by the decay of a bound electron. Since *K* and *L* fluorescence yields are so small for aluminum, most of these vacancies are filled by Auger processes. Hence, the radiation absorbed in the backside region tends to be predominantly channeled into ionization along with thermalization via the ejected Auger electrons, i.e., the ejected-electron energy is arbitrarily dumped into the thermal reservoir in this calculation.

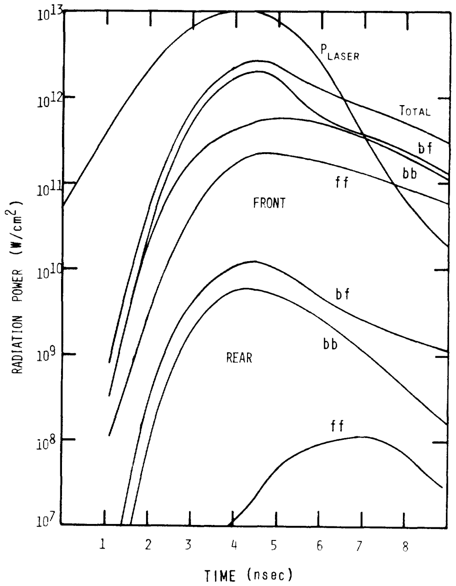

FIG. 4. Time evolution of the laser power and total radiative power of the laser-heated foil. The total power is also separated into lines (bb), radiative recombination (bf), and bremsstrahlung (ff) in the forward and rearward directions.

B. Energy transport in the foil

To elucidate the role played by radiation in the transport of energy through the foil, a discussion of both the spatial and temporal distribution of the emission is necessary. Although a large fraction of the radiated photons are reabsorbed before ever escaping the plasma, much can be learned from the gross characteristics of the radiation that does get out. In Fig. 4, we show the total forward and backward radiation power as a function of time, along with the temporal laser pulse shape. The emission in the forward direction is typically two orders of magnitude more intense than that from the backside. Also shown in the figure are the three components of the total: bound-bound (line emission), bound-free (radiative recombination emission), and free-free (bremsstrahlung) radiation. Both front and back directions are dominated by bound-free processes, while bremsstrahlung plays only a minor role in the foil energetics, accounting for only 10% of the total emitted radiation. The roughly $\frac{1}{2}$ nsec delay between the peaks in the laser profile and the radiation pulse is of no significance other than representing the difference between the temporal laser power and the integrated power or laser energy deposition. Thus, the plasma radiation responds quickly to changes in energy deposition. This is rather what one would expect from the frontside emission, but it is not so intuitive as regards the backside radiation, where one might expect some "lag time" between laser and radiation power. It will be shown later that the bulk of the calculated rearward emission is comprised of secondary *K*-line x rays above a kilovolt shining through the foil from the blowoff and transition regions and hence responds quickly to laser power. Compare this with the backside bremsstrahlung component which is born in the dense rearside of the foil; the response is much slower for these photons which are truly emanating from the rear of the foil. However, with only a calorimeter or bolometer at his disposal, an experimentalist would see only the response of the more energetic shine-through component from the front. Of course, with thicker foils, the rearside spectrum changes accordingly, and fewer x rays from the front penetrate through the foil to overshadow the true backside emission.

An important question we wanted to address with this model was "How much of the backside heating is attributable to thermal conduction, how much to radiation, how much to shocks, etc.?" To answer this, a graph of the spatial variation of several pertinent parameters can be illuminating. In Fig. 5 is shown a snapshot (at a time near peak emission) of the plasma temperature, density, and net radiative cooling, along with the position of the laser deposition critical surface (the original foil position was at $d=0$). The radiational cooling follows the density profile closely in the blowoff region, whereas it drops sharply just forward of the ablation surface where the plasma temperature starts to fall off. Further into the foil, the plasma becomes heated by radiation, i.e., it absorbs more energy from photons than it emits. By comparing the values for the rate of heating, we find that radiation is *two to three orders of magnitude* more effective than thermal conduction in the dense backside region. In addition, the assumed laser irradiance was low enough that only a small shock wave was propagated and contributed little to the backside heating. The radiational heating of the backside region can be seen clearly in the temperature curve. Without radiation, the curve would drop smoothly to near zero at the backside; in Fig. 5, however, a noticeable hump is present near the original foil position and the temperature drops to about 5 eV at the backside. The flat temperature profile in the blowoff region is a consequence of the one-dimensionality of the model, since it cannot take account of the actual-two-dimensional cooling of the ablating plasma.

Another point of interest in the energy transfer physics is the temporal behavior of the backside temperature; this is shown in Fig. 6 along with the laser pulse shape. The lag time between the laser peak and the peak in the backside temperature is about 2.5 nsec, and the temperature reaches a maximum of about 7.5 eV. These values are in reasonable agreement with those quoted by McLean *et al.*,[2] although their measurements were taken for slightly different laser and foil parameters than ours. Knowing that radiation is responsible for backside heating, one would expect the temperature there to have a temporal behavior similar to the rearward radiation profile. However, the total backward radiation pulse (as well as the bound-bound and bound-free emission) is characteristic of the emission which *passes through* the backside, not what is *stopped* in the backside. The backside bremsstrahlung tells the story of the rearside temperature history, since it truly originates in the backside; this can be seen in Figs. 5 and 6. What causes the time lag, then? Why does the backside not respond immediately to the frontside radiation shining back into the foil? The answer is that ionization-dependent inner-shell opacity controls the time dependence of the backside temperature. A simpler way of stating this is that, like a combustion wave, radiation incident on the backside region must first "burn" its way through to the rear surface before it can heat it via the photoionization-Auger-thermalization cycle. "Burn" in this context means "ionize," since the inner-shell opacity must be reduced before the radiation can penetrate deeper into the plasma. How is this accomplished in the laser-heated foil? Since the strongly emitted features of a material are also strongly absorbed by that material when cold and dense, a changing temperature profile on the frontside will not appreciably alter the heat-

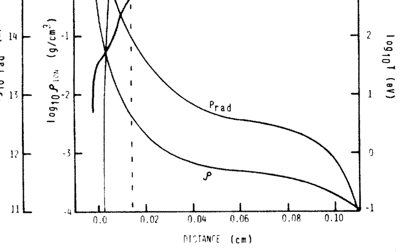

FIG. 5. Temperature, mass density, and radiative cooling as a function of position in the laser-heated foil, at a time near peak radiative emission (~5 nsec).

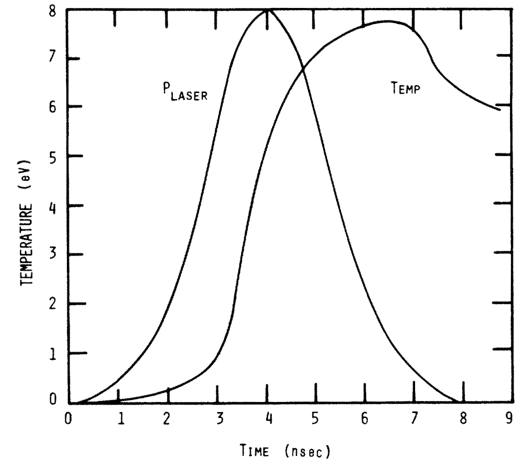

FIG. 6. Backside temperature of the laser-heated foil as a function of time. The laser power is shown for reference.

ing by shifting the intense features of the spectrum away from absorption edges. What does occur, however, is the shifting of absorption edges. As the region between the ablation surface and the rear surface slowly heats up, it ionizes, causing the absorption edges to shift according to Fig. 2. In this way, radiation from the front slowly burns its way through to the rear surface. Thus, the upward drift in rearside temperature after termination of the laser pulse reported by McLean *et al.*[2] is probably not due to thermal conduction, but, more likely, is due to "ionization burn-through" of the dense backside region by secondary x rays and xuv photons from the ablation and blowoff regions.

The temporal behavior of the backside temperature can have serious consequences on fuel preheat in laser pellets, and a common question is when the backside becomes hot enough to heat the fuel. Perhaps another question to consider is the effect of the prompt shine-through radiation on the fuel. Depending on the pellet shell material (which dictates the emitted spectral distribution), and the radiative absorption characteristics of the fuel, radiation preheat could be a more serious threat to efficient fuel compression on a low isentrope than backside plasma temperature.

One final point in regard to the energy transfer through the foil is the energy partitioning. In Fig. 7 are shown the various energy terms as they progress in time. These include the laser deposition, particle kinetic energy, radiation energy loss, internal energy, and energy of the ions due to ionization and excitation. The final percentages at the end of the run ($t = 8.3$ nsec) are shown in Table II. Most of the energy has been converted into kinetic energy of the foil, as it is accelerated by the ablating plasma in the blowoff region. However, over a quarter of the absorbed energy has been radiated away, most of it out the front of the foil. The internal energy peaks near the maximum of the laser pulse and drops thereafter as the plasma commences cooling. The ionization energy has been maintained at a constant level since the peak of the laser pulse, indicating little ion recombination has taken place during this time. This seems a bit contradictory in view of the decreasing internal energy. Most of the ionization energy is in the dense backside regions of the foil, where plasma cooling changes the temperature only a few electron volts; this has little effect on the ionization state there. On the other hand, the thermal energy is more evenly distributed throughout the backside and transition zones where the cooling has more noticeable effects on the internal energy. Ionization energies in the transition zone are larger and a large decrease in the temperature there will greatly decrease the total plasma potential energy.

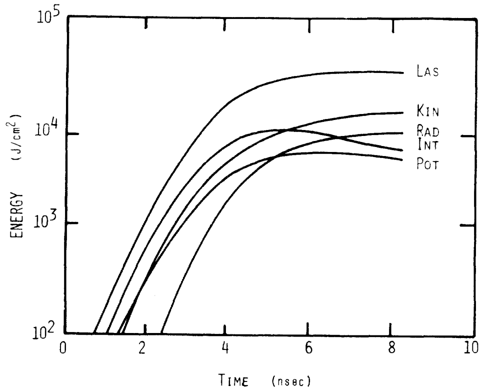

FIG. 7. Laser-foil energy partitioning as a function of time, including laser deposition (LAS), kinetic energy (KIN), radiative cooling (RAD), internal energy (INT), potential energy (POT).

TABLE II. Energy partitioning of the laser-heated foil at the end of the theoretical simulation ($t = 8.3$ nsec).

Mechanism	Energy (joules)	Percentage
Laser deposition	2.94×10^4	100%
Kinetic energy	1.20×10^4	40.8
Radiative loss	7.76×10^3	26.4
Internal energy	5.34×10^3	18.2
Potential energy	4.29×10^3	14.6

C. Spectral energetics

In this section we analyze the details of the forward and rearward spectral emission and attempt to explain how radiation is transported through the foil. The emphasis here will be on the energetics of the gross spectrum, whereas spectral diagnostics are discussed in Sec. III D.

Shown in Fig. 8 is the total, time-integrated radiation spectrum from the frontside of the foil, over a range from 10 eV to 10 keV. There are several interesting details in this plot which merit further discussion. At low photon energies, the emission is predominantly bremsstrahlung; to illustrate, the free-free portion of the spectral intensity is shown as a broken dotted curve. Also, few lines are present below 30 eV, since photons from most lines in this range are born of lower ionization stages found in the dense backside region, and are strongly attenuated before reaching the front of the foil. Above 50 eV, many strong lines are present, sitting on a continuum baseline made up of recombination radiation. This bound-free component is also shown in the figure as a broken curve. Between 450 eV and 1.5 keV, no lines are present since this range falls in

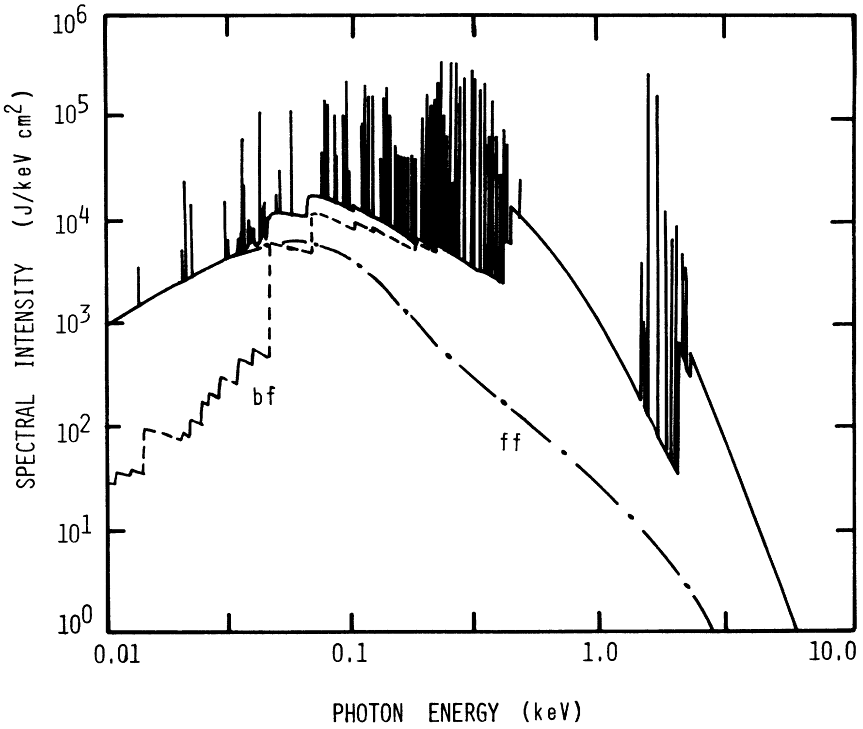

FIG. 8. Full time-integrated spectrum from the frontside of the laser-heated foil. Also shown are the bound-free (bf) and free-free (ff) components of the radiation.

the energy gap between the *K* and *L* lines; the emission here is bound-free radiation from heliumlike aluminum. Above 1.5 keV is the *K*-shell radiation: *Kα* emission and hydrogenlike and heliumlike lines. The continuum level rises at energies above 2 keV due to the recombination edges of Al XIII and Al XIV. A more detailed analysis of the *K*-shell spectrum will be presented in the diagnostic section following.

An interesting question that often occurs in spectroscopy is the degree to which the spectra change during the time development of the plasma. If one could substantiate that the "snapshot" power spectrum at a time near peak emission was qualitatively similar to the time-integrated spectrum, the frequently used approach of inferring that the plasma parameters obtained by diagnosing the time-integrated spectrum are typical of the plasma at peak emission could be validated. In Fig. 9, we show a snapshot of the frontside spectrum at a time near peak emission. Comparison with Fig. 8 shows little qualitative difference in terms of the slope of continuum features and strong line intensities. The only noticeable difference is the slope of the Al XII recombination continuum between 0.45 and 1.5 keV. In general, most of the frontside snapshot spectra that were generated (at various times during the main emission pulse) looked qualitatively similar to the time-integrated spectrum; essentially only the intensity levels change slightly with time. In the next section, the *K*-shell x-ray spectra will be examined in detail to assess the finer discrepancies between time-integrated and time-resolved spectra.

We now turn our attention to the radiation spectrum from the rearside of the foil. The full time-integrated spectrum is shown in Fig. 10, and substantial differences are found compared to the frontside emission shown in Fig. 8, the most noticeable being the absence of radiation between 80 and about 650 eV. The opacity due to inner-shell photoionization strongly attenuates all photons in this energy band. Below the *L* absorption edge, two superimposed features are seen: (1) The continuum radiation emanating from the dense backside region and approximating a Planckian function at low temperature (about 6.0 eV), (2) a small recombination feature, cut off at the *L* edge, consisting of photons from the transition region, which manage to escape through the backside. The high-energy component of the spectrum is all shine-through radiation from the frontside blowoff region and consists of attenuated *K* lines and bound-free continuum from *L* and *K* electrons. Notice the distorted appearance of these continuum features due to opacity, which

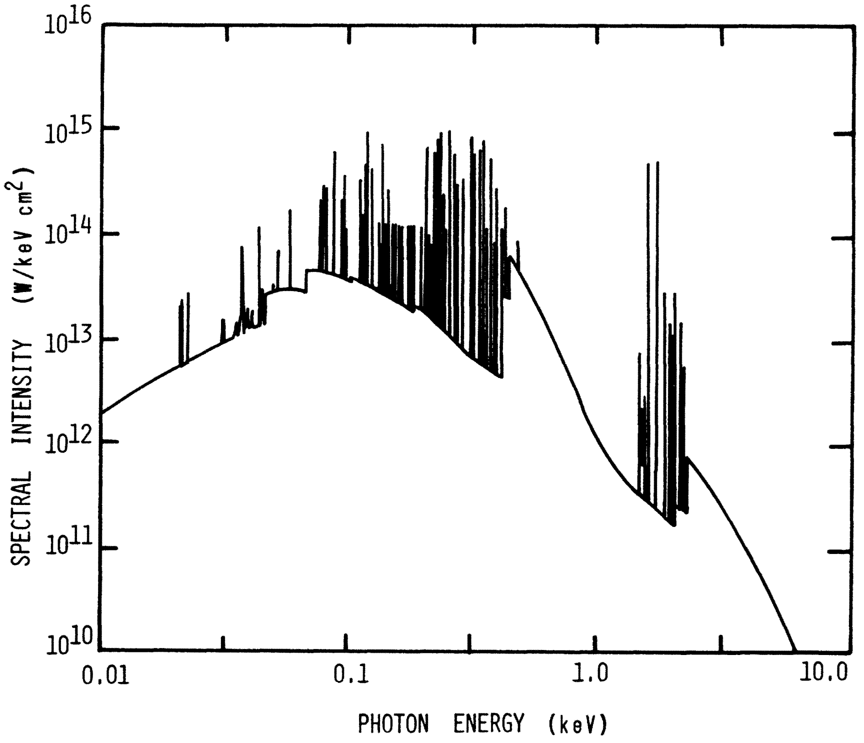

FIG. 9. Full snapshot spectrum from the frontside of the laser-heated foil at $t = 4.59$ nsec.

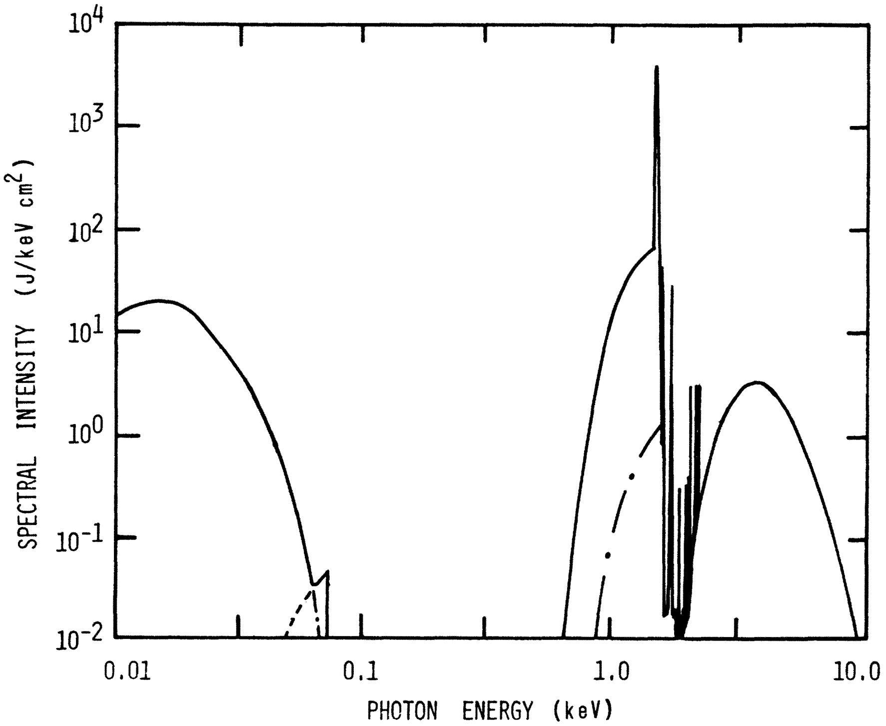

FIG. 10. Full time-integrated spectrum from the rearside of the laser-heated foil. Bound-free contribution is shown as a dashed line, while free-free is shown as alternating dots and dashes.

shifts the frequency at which most bound-free photons escape from the actual recombination edge frequency. The shift can be approximated by the expression

$$E_{\text{shift}} \approx E_0^{3/4}(3\tau_0 kT)^{1/4} , \tag{23}$$

where $E_0 = h\nu_0, \nu_0$ is the edge frequency, and τ_0 is the optical depth at the recombination edge. This calculated spectrum was verified by comparing it with the predicted instantaneous emission spectrum from a more detailed transport calculation[44] which solves the exact equation of transfer for a large-frequency grid, and agreement between the two models was excellent. Superimposed on the continuum is the $K\alpha$ emission which appears as a single large spike with the coarse resolution of Fig. 10. The $K\alpha$ radiation comes from regions where K-shell photons are strongly absorbed by inner-shell processes. Only the low-energy continuum radiation constitutes actual backside region emission, from within a few optical depths of the rear surface. The other features are shine-through from beyond the ablation surface.

Although few qualitative differences were found in time-integrated and time-resolved spectra in the frontward direction, substantial differences are seen in the rearward spectra. In Fig. 11, the full backside snapshot power spectrum is shown at five times during the emission pulse, and significant differences are evident. At t_1 (3.0 nsec), only L-shell bound-free emission is strong, appearing just below the K edge. The K-shell lines and continuum are barely evident. The sharp spike at 1.5 keV is the blend of $K\alpha$ lines. At t_2 (3.9 nsec) and t_3 (5.0 nsec), two changes are seen: (1) continuum radiation appears at low photon energies as the backside plasma begins to heat up, (2) more K-shell radiation is emitted and the emission penetrates the dense plasma more easily as the inner-shell opacity is slowly reduced by burnthrough in the transition zone and forward-most zones of the backside region. Also shown in these spectra is the blackbody (BB) curve (broken line) corresponding to the temperature of the last backside zone. The actual emission in these spectra tracks the BB curve very well up to the L edge. This is due to the strong opacity at these low photon energies, predominantly free-free, but with a non-negligible bound-free opacity contribution. Thus, at low frequency the backside plasma looks like a blackbody emitter and validates the procedure of McLean *et al.* in obtaining backside temperatures from time-dependent spectroscopy at several low photon frequencies and fitting the result to the appropriate BB profile.

At t_4 (6.4 nsec), the frontside blowoff is beginning to cool due to expansion and reduced laser power,

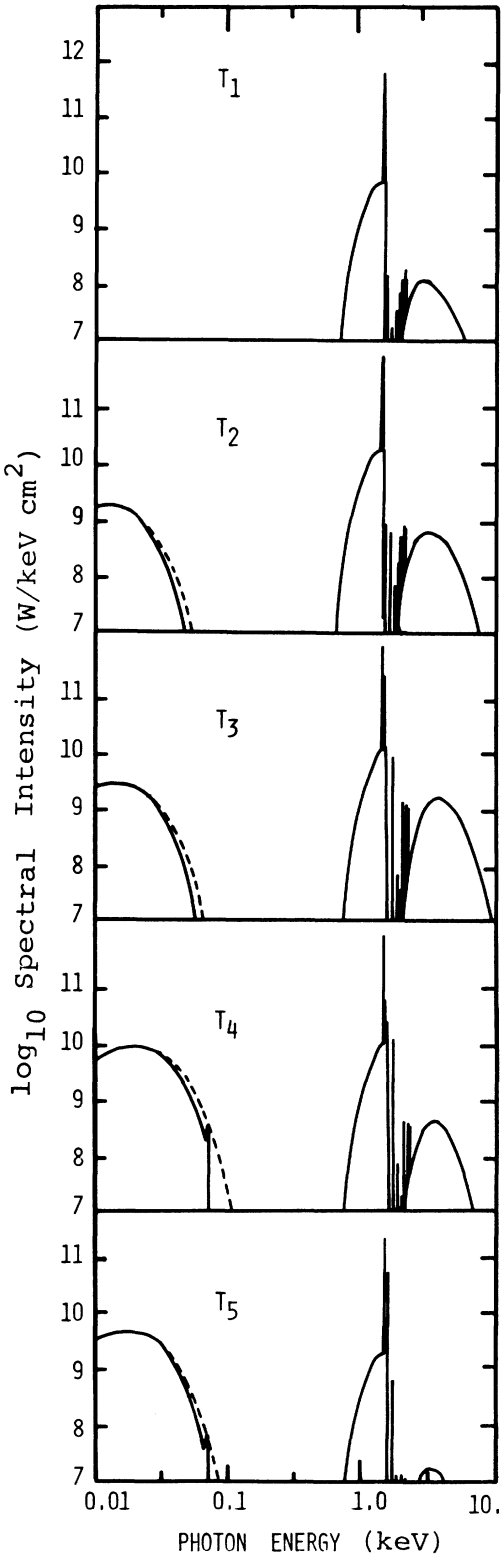

FIG. 11. Full snapshot spectra from the rearside of the laser-heated foil at five different times: $T_1 = 3.0$ nsec, $T_2 = 3.9$ nsec, $T_3 = 5.0$ nsec, $T_4 = 6.4$ nsec, $T_5 = 8.4$ nsec.

which is evident from the decrease in the *K*-shell shine-through. The transition zone is still maintaining its temperature, however, and the *L*-shell continuum, just below the *K* edge, is still strong. The bremsstrahlung intensity level at low frequency is still increasing since the backside temperature reaches a maximum at 6.5 nsec (see Fig. 6); in addition, it still maintains close proximity with the Planck function, determined by the backside temperature. Also present is a very weak bound-free continuum feature just below the *L* edge, which rises to the vicinity of the BB curve. It should be emphasized here that the BB curve corresponding to the rear surface temperature does not represent an upper limit to this continuum emission, since this radiation is emitted from several optical depths into the backside region and at frequencies where the plasma is not a perfect absorber. The time-integrated spectrum in Fig. 10 most resembles the snapshot spectrum at this time.

Finally, at t_5 (8.4 nsec) the *K*-shell contribution is negligible, and only bremsstrahlung, *L*-shell bound-free continuum, and $K\alpha$ emission are present. Note that the *L* edge is still a major absorption mechanism, as evidenced by the large gap in the emission. From a "plasma" point of view, this spectral gap is an indication that the laser has still not burned through the foil, since the foil backside region has yet to be heated to high temperatures. From a radiation standpoint, however, burn-through is not so clearly defined, since secondary emission from the frontside is the strongest radiational component through the backside and it commences promptly after laser-plasma interaction begins. Thus, if the absorption cross section for the fuel (or intermediate tamper) is large at frequencies corresponding to this shine-through emission, and the shine-through radiation is sufficiently intense, as in thinner foils, parameters such as foil burn-through time can be of minor consequence when considering target preheat.

To more quantitatively assess the radiative output of this laser-foil interaction, the frontside and backside radiative components are shown in Table III; the emission is separated by both energy bins and atomic mechanism as well as direction, and is expressed as a percentage of the total radiation in the appropriate direction. The total forward emission is approximately a factor of 100 times more intense than the total rearward emission. For the most part, the table is self-explanatory. A few points need to be emphasized, however. The low-energy bremsstrahlung from the backside accounts for less than a percent of the rearward emission; almost all lies in photons above a kilovolt. The bremsstrahlung component (both front and back) as a whole is energetically unimportant, comprising only about 10% of the foil radiation, while radiative recombination is the most important radiative process. Conversion efficiencies are often numbers of interest in experiments of this sort. The total laser-to-radiation conversion efficiency was 26.4%, hence, from Table III, the conversion to x rays above 1.5 keV is only 5.3%, and above 0.5 keV it is 12%.

D. *K*-shell diagnostics

Many previous papers[45] have dealt with the subject of *K*-shell radiation diagnostics in dense plasmas. However, most have employed stationary atomic models uncoupled from the plasma dynamics for the sake of simplicity. With this model we are able to make detailed comparisons between time-integrated and time-resolved spectral emission for the *K*-shell region to determine what portion of the plasma evolution is characterized by the time-integrated spectrum. Granted, with the recent advent of spectroscopically resolving x-ray streak cameras, this new advanced technology has made it possible to obtain time-resolved *K*-shell spectra for the first time. However, this will be a successful diag-

TABLE III. Total time-integrated radiation energy in the forward and rearward directions, separated by various photon energy bins and by the atomic process responsible for the emission (values are given as percentages of the total in that direction).

Photon	Forward spectrum				Backward spectrum			
energy (eV)	bb	bf	ff	total	bb	bf	ff	total
1–40	0.0	0.1	1.2	1.3	0.0	0.0	0.6	0.6
40–125	1.2	8.0	5.1	14.3	0.0	0.3	0.0	0.3
125–300	7.0	11.3	2.2	20.5	0.0	0.0	0.0	0.0
300–500	3.3	14.0	0.5	17.8	0.0	0.0	0.0	0.0
500–1560	0.6	25.1	0.3	26.0	30.9	50.9	0.0	81.8
1560–5000	15.6	4.3	0.2	20.1	1.2	16.1	0.0	17.3
Total	27.7	62.8	9.5	100.0	32.1	67.3	0.6	100.0

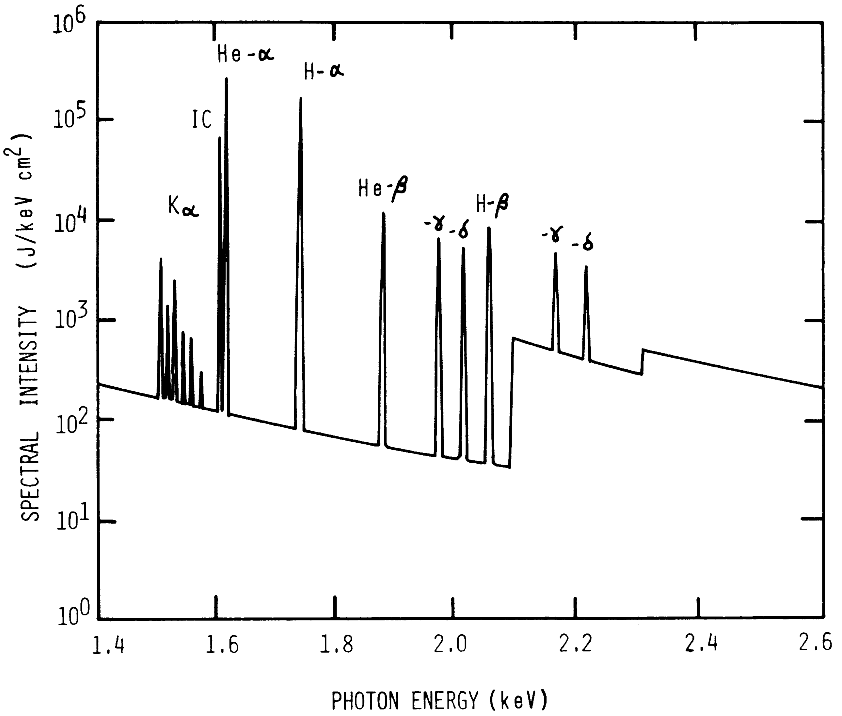

FIG. 12. Time-integrated *K*-shell spectrum from the frontside of the laser-heated foil.

nostic tool only if intensities are sufficiently high. Other valuable diagnostic techniques, e.g., impurity doping,[46] tracer-dot implantation,[47] and slitting to obtain spatially resolved information, often limit the measured intensity of the emission, making time-resolved measurements difficult and uncertain. Thus, the relationship between time-integrated measurements and the evolution of various plasma parameters of interest is still an important unanswered question.

The time-integrated *K*-shell frontside spectrum, shown in Fig. 12, contains Rydberg series lines from hydrogenlike Al XIII and heliumlike Al XII, resulting from the spontaneous decay of *np* states ($n \leq 5$) to the 1*s* orbitals. In addition, the density-sensitive $1s^2(^1S)\text{-}1s\,2p(^3P)$ intercombination (IC) line is also shown, as well as the two recombination continua Al XIV-to-Al XIII and Al XIII-to-Al XII, seen as sharp edges above 2 keV. At slightly lower energies, the $K\alpha$ series of lines is shown; as stated earlier, they are treated as optically thin in this study. Thus, their intensities here are identical to those predicted in the rearward spectrum, and it will suffice to discuss their relative intensities as seen in Fig. 12 without showing a *K*-shell backside spectrum.

In order to allow for comparison, the frontside snapshot spectra for several times are shown in Fig. 13. Since the real *K* lines (as opposed to the $K\alpha$ lines) are valence electron transitions from highly ionized aluminum, they are emitted entirely from the frontside blowoff and the transition zone just in back of the critical surface. As thermal conduction of deposited laser energy back into the foil becomes ineffective as a heating mechanism, the temperature drops and the *K* lines are no longer emitted; this probably occurs at some point between the critical and ablation surfaces, at a temperature around 150—200 eV. Hence, the *K*-line emission is characteristic of somewhat dense as well as rarefied regions of the foil plasma. Limiting this first discussion to the *K* lines, very little difference is evident between the five spectra in Fig. 13 and the one in Fig. 12. The intensities fall off at t_5 (7.35 nsec), but relative line intensities vary only slightly. To magnify these differences, we have plotted three line ratios commonly used for plasma diagnostics as a function of time in Fig. 14. Curve 1 is the H-β/He-$\delta$$[1s\text{-}3p/1s^2\text{-}1s\,5p(^1P)]$ ratio, curve 2 is the H-α/He-$\alpha$$[1s\text{-}2p/1s^2\text{-}1s\,2p(^1P)]$ ratio, and curve 3 is the IC/He-$\alpha$$[1s^2\text{-}1s\,2p(^3P)/1s^2\text{-}1s\,2p(^1P)]$ line ratio. The first two are temperature sensitive, while the third is density sensitive. A complete discussion of these line diagnostics in isothermal, isodense plasmas can be found in Ref. 18, while the effects of density and temperature gradients on these ratios has been described in Ref. 19.

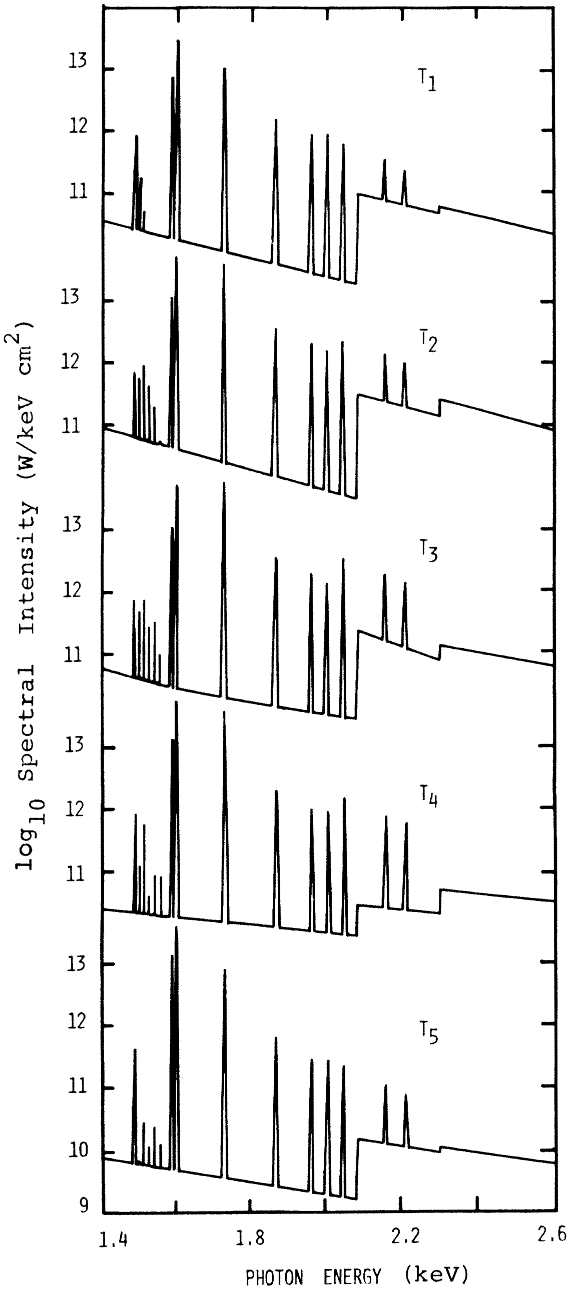

FIG. 13. K-shell snapshot spectra from the frontside of the laser-heated foil at five different times: $T_1=2.9$ nsec, $T_2=3.9$ nsec, $T_3=4.6$ nsec, $T_4=5.9$ nsec, and $T_5=7.4$ nsec.

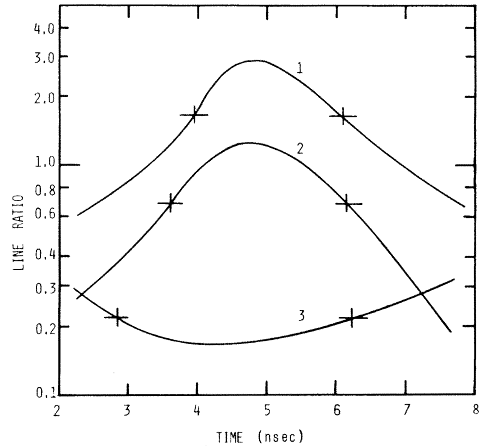

FIG. 14. Behavior of various K-shell line ratios as a function of time: curve 1 H-β/He-δ, curve 2 H-α/He-α, curve 3 IC/He-α.

What we seek to determine here is the effect of time integration on these diagnostics. Namely, what can we expect to learn from a time-integrated spectrum which has been obtained from a plasma which changes significantly during the radiation pulse time? Examining the time behavior of curves 1 and 2, they display maxima at 4.8 nsec when the blowoff plasma is the hottest and the greatest abundance of hydrogenlike aluminum ions, relative to heliumlike ions is attained. Curve 3 shows a minimum corresponding to the peak plasma density in the blowoff region, which occurs at 4.2 nsec, slightly earlier than the time peak temperature is reached. Superimposed on the curves are crosses which indicate the values for these ratios from the time-integrated spectrum in Fig. 12. It seems to indicate that the time-integration averages the values obtained for plasma parameters over a time period comparable to the total radiation pulse width, which is what one would intuitively expect rather than a significant weighting by the ratios in either the pre- or post-maximum direction. However, the more interesting question is what is the *difference* in temperatures (or densities) between the peak values attained in the plasma and those indicated by the time-integrated diagnostics? Using theoretical line-ratio calculations generated for the study in Ref. 19, ratios 1 and 2 indicate time-integrated values for the temperature roughly *200 eV lower* than those indicated by a time-resolved spectrum at the time of maximum temperature. Similarly, the time-integrated density as determined by ratio 3 is 25% lower than that predicted by the time-resolved spectrum at maximum emission time. What impact does this have on spatially and temporally integrated diagnostics? As seen in the study on plasma gradients, a laser-heated slab plasma will be diagnosed significantly cooler than the actual spatially averaged temperature due to spatial integration of the line spectrum over gradients normal to the target. Couple this with the result above due to time integration, and the net result from spectral diagnostics can be expected to be several hundred electron volts below the maximum average temperature attained in the plasma. Combined effects of spatial and temporal integration on the density determination are nearly as strong, and the values obtained are at least a factor of 2 lower than the maximum average density attained in the K-shell emitting region.

Our final goal in this work was to make some definitive contribution in the use of $K\alpha$ emission to diagnose cold, dense matter. In this initial effort to study these features, the $K\alpha$ emission was not transported; hence, every K vacancy that was created resulted in a measured $K\alpha$ as dictated by the appropriate fluorescence yield. The $K\alpha$ emission is seen most clearly in Fig. 12, the time-integrated, frontside, K-shell spectrum. As was stated in Sec. II, each ionization stage will emit $K\alpha$ radiation at a different frequency, since the shielding due to outer electrons is different. Since the first four ions have similar ionization energies, the $K\alpha$ lines corresponding to them are usually unresolvable, and appear in Fig. 12 as a single strong line, followed by the other five $K\alpha$ lines included in this model from the remaining ionization stages. The time evolution of these lines is represented in Fig. 13, where the higher lines are seen to grow in intensity and then fall off as time progresses. This can be seen more clearly in Fig. 15, where the $K\alpha$ intensities are plotted as a function of time. The actual time-integrated line ratios, relative to the intensity of the first and strongest $K\alpha$ feature are 1:0.23:0.59:0.12:0.11:0.03.

At the outset, we anticipated we would be able to make quantitative statements about the dense plasma based on the time-integrated $K\alpha$ emission. In fact, this proved to be quite difficult, since each line is emitted over a widely varying pulse width as seen in the figure. This pulse width corresponds to the period during which the respective ionization state is in abundance somewhere in the dense plasma region. The reason the dense plasma region dominates is a function of the inner-shell opacity. At densities much below solid, the creation rate of K-shell vacancies per unit volume at this laser power is not large enough to generate $K\alpha$ lines intense enough for measurement. However, Fig. 15 shows that to fully understand the $K\alpha$ radiation diagnostics, the time history of the lines must be known, hence, time-resolved spectroscopy is probably necessary. In addition, for this information to be useful, one must know from what regions of the plasma these lines emanate. If they all had come from the dense region very close to the foil backside, as we initially anticipated, Fig. 15 would look like a typical ionization abundance curve versus plasma temperature, with each ionization stage dominating at later and later times, until the backside began to cool, whence $K\alpha$ from lower ionization stages would reappear in reverse order. Since this is not the case in Fig. 15, the emission region must be different from what we had originally guessed.

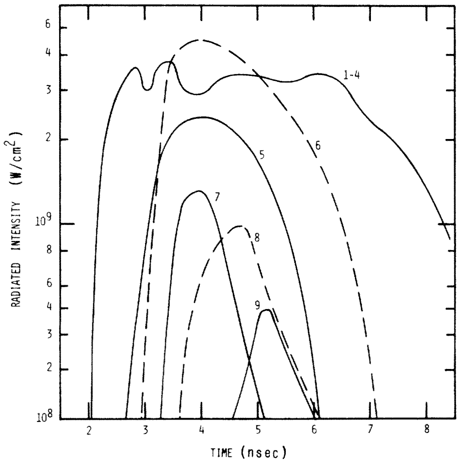

FIG. 15. Time behavior of the various $K\alpha$ line intensities in the laser-heated foil (optically thin approximation). Numbers refer to the atom or ion before photoionization occurs (5≡Al V or Al^{4+}).

From the time history of these lines we see that successive ionization stages do "turn on" at progressively later times, as initially expected. However, the lower ionization stages do not disappear and reappear later, but sustain themselves over significant time intervals. The sustained nature of the lower ionization stages is due to the fact that the $K\alpha$ lines are coming from different regions of the plasma. The lowest ionization stages are coming from the far backside, while the higher ionization stages emit $K\alpha$ lines almost to the ablation surface in the transition zone. This is an interesting phenomenon from a diagnostic point of view and there are basically two reasons for it. Obviously, the temperature increases as one moves into the plasma from the backside, hence, the ionization abundances change predictably. Second (and a very necessary criterion), the K absorption edge shifts to higher photon energies with temperature, allowing the intense helium-like resonance line, for example, from the frontside to penetrate deeper and deeper into the plasma as it heats up. The Ly-α line, on the other hand, will be attenuated along with the other Rydberg series lines by the first dense zone it encounters, just beyond the ablation surface, since the K edge rarely shifts that much in the dense plasma region. Therefore, instead of yielding diagnostic information about the temperature of the far backside of the foil, we find that, knowing the $K\alpha$ line time histories, one can determine the dominant ionization stage (and, therefore, the approximate temperature) of the plasma region in the vicinity of the *ablation surface* and how that temperature behaves in time. From Fig. 15 we know that at its hottest point, near $t = 5$ nsec, the region in the vicinity of the ablation surface was mostly Al VIII and Al IX. Hence from CRE aluminum ionization abundance plots (see, e.g., Ref. 18), the temperature must have reached approximately 50–60 eV at this time. At the peak of the laser pulse ($t = 4$) nsec), on the other hand, Al VII was dominant in that region, and the temperature was probably nearer to 40 eV at the ablation surface.

Of course, opacity effects may disturb the relative intensities of these lines, and work is underway to include these effects in our model. However, their time behavior appears to be more significant than their relative intensities as a useful diagnostic tool.

IV. CONCLUSIONS

The purpose of this investigation was to study the radiation dynamics of a medium-z material, heated to x-ray emitting temperatures by a laser. Although some physical mechanisms were not included in the theoretical model, the laser power was chosen so as to minimize the effect of these processes and allow us to concentrate on the radiative aspects of the problem. Therefore, we believe this model to be quite adequate to allow us to study the processes emphasized in this report in a detailed way and draw meaningful conclusions.

Several interesting conclusions were drawn from this work which are worthwhile summarizing. Our primary goal was to determine how important radiation was as an energy transport mechanism. For the conditions here, i.e., 10^{13} W/cm^2 glass laser pulse with a 3 nsec pulse width incident on an 8 μm thick aluminum foil, radiation was several orders of magnitude more efficient in transporting energy past the ablation surface than the second most important process, thermal conduction. (Recently, Yaakobi *et al.*,[35] in an interesting study of intense 0.35 μm laser light on saran targets, concluded that radiation, not suprathermal electrons, was responsible for heat transport past the ablation surface.) It was found that the heating in this region was caused by photoionization of inner-shell electrons in the dense backside plasma and that the incident photons transporting the energy consisted of down-converted xuv photons ($h\nu < 1$ keV) from the transition zone as well as secondary x-rays ($h\nu > 1$ keV) from the frontside blowoff region. Thus, the backside heating process is a complex one, not easily characterized by simpler models of the dense plasma, driven solely by K lines. The delay in the backside temperature rise after termination of the laser pulse was found to be totally radiative in nature and not attributable to thermal conduction eventually burning through the plasma. As secondary xuv and soft x-ray photons from the frontside and transition zones heat the dense, cold backside plasma, it slowly heats up and ionizes, shifting absorption edges to higher photon energies. This allows deeper and deeper penetration of these photons with time, resulting in a moving ionization (or temperature) front toward the rear of the plasma. Of course, the process is a continuous one across the entire spectrum, so the far backside temperature rises smoothly in time as increasing numbers of photons are able to penetrate. Hence, the concept of "prompt" x-ray heating of the backside is probably incorrect in all but very thin foils, and in these cases, thermal conduction will most likely dominate the heating. Summing up, "ionization burn-through" proved to be most important to radiative heating of the backside for the conditions considered here.

Concerning the general nature of the emitted radiation, about $\frac{2}{3}$ can be attributed to bound-free atomic processes (radiative recombination), about $\frac{1}{4}$ to line emission, and only $\frac{1}{10}$ to bremsstrahlung photons. The radiation directed out the frontside of the plasma was almost 100 times more intense than that in the rearward direction, but this will be strongly dependent on the foil thickness and laser wavelength. The rearside spectrum consists of a low-energy continuum, emitted directly from the backside region after the peak in the laser pulse, along with a higher energy prompt component shining through from the frontside and consisting of K lines and continuum and some L-shell continuum from the transition zone. In addition, strong $K\alpha$ features were present, emitted in the dense plasma region. The rearside low-energy continuum closely follows the curve for a blackbody emitter at the rearside temperature, up to photon energies well below the L edge, and the ion populations in the dense plasma are very nearly in local thermodynamic equilibrium (LTE). Depending on the absorption characteristics of the fuel constituents in a microballoon, this transmitted radiation may or may not represent a serious source of preheat in the fuel region.

Two main points are to be made regarding spectroscopic plasma diagnostics. First, the time-integration of the spectral emission has a large effect on line-ratio diagnostics from laser-produced plasmas. The final time-integrated intensities of K-shell emission lines indicated average temperatures and densities significantly lower than the maximum actually achieved in the plasma for these conditions. Thus, time-integration coupled with spatial gradients in these plasma parameters can have a serious effect on spectroscopic techniques used to diagnose them.

Finally, it was found that the *Kα* lines can be a promising diagnostic tool in laser-produced plasmas. Since these features are emitted throughout the dense backside region, all the way up to very near the ablation surface, their time histories can be used to determine the temporal behavior of the electron temperature in the vicinity of the ablation surface. In principle, crystal-diffraction streak camera spectroscopy should be able to track the time-dependence of the *Kα* components of the higher ionization stages in the dense plasma, and convert this information to temperature using ion abundance plots at high densities. Of course, no opacity effects were included when transporting the *Kα* in our model, and fast electrons can also create *K* vacancies which give rise to these lines, but these factors should not in principle detract from the use of the *Kα* lines to determine the time evolution of the plasma temperature deep in the plasma. In fact, the *Kα* features emitted near the ablation surface may be more easily detectable in the forward spectrum than in the rearward.

In conclusion, we have tried to show the importance of plasma radiation to the energy transport in laser-heated foils. The radiation model employed in this study is one of the most detailed ever to be used in such a way, incorporating a comprehensive treatment of level population dynamics and radiation emission and transport. Although this model may lack the detail of other hydrodynamic codes used to address this problem, we believe our fluid treatment of the plasma medium to be quite sufficient to study the phenomenon of laser-foil interaction, and the conclusions drawn are valid ones for the initial conditions assumed. More detailed analysis of the comparison between various ionization-radiation models and the impact of neglecting radiation on the plasma modeling is the subject of another study presently nearing completion, and will be presented in another paper to follow.

ACKNOWLEDGMENTS

The authors would like to thank P. C. Kepple and H. R. Griem for helpful discussions and suggestions regarding the manuscript. This research was supported by the U.S. Defense Nuclear Agency.

---

[1] B. H. Ripin *et al.*, Phys. Fluids 23, 1012 (1980); 24, 990 (1981).

[2] E. A. McLean *et al.*, Phys. Rev. Lett. 45, 1246 (1980).

[3] J. A. Stamper *et al.*, J. Appl. Phys. 52, 6562 (1981).

[4] B. H. Ripin, E. A. McLean, and J. A. Stamper, Phys. Fluids 25, 2128 (1982).

[5] H. Nishimura *et al.*, Phys. Rev. A 23, 2011 (1981).

[6] H. Nishimura, M. Yagi, F. Matsuoka, K. Yamada, T. Yamanaka, S. Nakai, and C. Yamanaka, Appl. Phys. Lett. 39, 592 (1981).

[7] J. W. Murdoch, J. D. Kilkenny, D. R. Gray, and W. T. Toner, Phys. Fluids 24, 2107 (1981).

[8] J. Nuckolls, L. Wood, A. Thiessen, and G. Zimmerman, Nature 239, 139 (1972).

[9] J. P. Boris and D. Book, J. Comput. Phys. 11, 38 (1973).

[10] D. Duston and J. Davis, Phys. Rev. A 23, 2602 (1981).

[11] D. R. Bates, A. E. Kingston, and R. W. P. McWhirter, Proc. R. Soc. London, Ser. A 267, 297 (1962).

[12] A. Burgess, in Proceedings of the Symposium on Atomic Collision Processes in Plasmas, Culham, England, Report No. 4818, 63, 1964 (unpublished); and A. Burgess, H. P. Summers, D. M. Cochrane, and R. W. P. McWhirter, Mon. Not. R. Astron. Soc. 179, 275 (1977).

[13] V. L. Jacobs, J. Davis, P. C. Kepple, and M. Blaha, Astrophys. J. 211, 605 (1977).

[14] W. J. Karzas and B. Latter, Astrophys. J. Suppl. Ser. 6, 167 (1961).

[15] V. L. Jacobs and J. Davis, Phys. Rev. A 18, 697 (1978).

[16] J. Davis, P. C. Kepple, and M. Blaha, J. Quant. Spectrosc. Radiat. Transfer 16, 1043 (1977).

[17] E. Oran and J. Davis, J. Appl. Phys. 45, 2480 (1974).

[18] D. Duston and J. Davis, Phys. Rev. A 21, 1664 (1980).

[19] D. Duston and J. Davis, Phys. Rev. A 24, 1505 (1981).

[20] J. P. Apruzese, J. Davis, D. Duston, and K. G. Whitney, J. Quant. Spectrosc. Radiat. Transfer 23, 479 (1980).

[21] C. W. Allen, *Astrophysical Quantities* (Athlone, London, 1955), p. 102.

[22] Frank Biggs and Ruth Lighthill, Sandia Laboratories Report No. SC-RR-71 0507, 1971 (unpublished).

[23] R. G. Reilman and S. T. Manson, Phys. Rev. A 18, 2124 (1978).

[24] E. Clementi and C. Roetti, At. Data Nucl. Data Tables 14, 177 (1974).

[25] J. Davis, R. W. Clark, D. Duston, and J. P. Apruzese (unpublished).

[26] B. Yaakobi, I. Pelah, and J. Hoose, Phys. Rev. Lett. 37, 836 (1976).

[27] K. B. Mitchell and R. P. Godwin, J. Appl. Phys. 49, 3851 (1977).

[28] A. Zigler, H. Zmora, and J. L. Schwob, Phys. Lett. 63A, 275 (1977).

[29] J. D. Hares, J. D. Kilkenny, M. H. Key, and J. G. Lunney, Phys. Rev. Lett. 42, 1216 (1979).

[30] R. D. Bleach, D. J. Nagel, D. Mosher, and S. J. Stephanakis, J. Appl. Phys. 52, 3064 (1981).

[31] E. Nardi, E. Peleg, and Z. Zinamon, Appl. Phys. Lett. 39, 46 (1981).

[32] E. Nardi and Z. Zinamon, J. Appl. Phys. 52, 7075 (1981).

[33] A. Hauer, W. Priedhorsky, and D. van Hulsteyn, Appl. Opt. 20, 3477 (1981).

[34] J. Mizui, N. Yamaguchi, T. Yamanaka, and C. Yama-

naka, Phys. Rev. Lett. 39, 619 (1977).

[35] B. Yaakobi, J. Delettrez, L. M. Goldman, R. L. McCrory, W. Seka, and J. M. Soures, Opt. Commun. 41, 355 (1982).

[36] For a more complete discussion, the reader is referred to the review article by W. Bambynek *et al.*, Rev. Mod. Phys. 44, 716 (1972).

[37] V. L. Jacobs, J. Davis, B. F. Rozsnyai, and J. W. Cooper, Phys. Rev. A 21, 1917 (1980).

[38] E. J. McGuire, private communication.

[39] P. J. Mallozzi *et al.*, in *Fundamental and Applied Laser Physics, proceedings of the Esfahan Symposium,* edited by M. S. Feld, J. Javan, and N. A. Kurnit (Wiley, New York, 1973), p. 165.

[40] D. Colombant and G. F. Tonon, J. Appl. Phys. 44, 3524 (1973).

[41] D. G. Colombant, K. G. Whitney, D. A. Tidman, N. K. Winsor, and J. Davis, Phys. Fluids 18, 1687 (1975).

[42] G. L. Payne, J. D. Perez, T. E. Sharp, and B. A. Watson, J. Appl. Phys. 49, 4688 (1978).

[43] H. Yasuda and T. Sekiguchi, Jpn. J. Appl. Phys. 18, 2245 (1979).

[44] J. P. Apruzese and R. W. Clark (unpublished).

[45] See, for example, the extensive reference list in the review article C. DeMichelis and M. Mattioli, Nucl. Fusion 21, 677 (1981).

[46] B. Yaakobi, D. Steel, E. Thorsos, A. Hauer, and B. Perry, Phys. Rev. Lett. 39, 1526 (1977).

[47] M. J. Herbst, P. G. Burkhalter, J. Grun, R. R. Whitlock, and M. Fink, NRL Memorandum Report No. 4812, Rev. Sci. Instrum. 53, 1418 (1982).